

## Reproducing kernel potential energy surfaces in biomolecular simulations: Nitric oxide binding to myoglobin

Maksym Soloviov and Markus Meuwly

Citation: *The Journal of Chemical Physics* **143**, 105103 (2015); doi: 10.1063/1.4929527

View online: <http://dx.doi.org/10.1063/1.4929527>

View Table of Contents: <http://scitation.aip.org/content/aip/journal/jcp/143/10?ver=pdfcov>

Published by the [AIP Publishing](#)

---

### Articles you may be interested in

[Revisiting the finite temperature string method for the calculation of reaction tubes and free energies](#)  
*J. Chem. Phys.* **130**, 194103 (2009); 10.1063/1.3130083

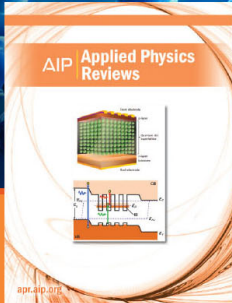
[Harmonic Fourier beads method for studying rare events on rugged energy surfaces](#)  
*J. Chem. Phys.* **125**, 174108 (2006); 10.1063/1.2363379

[A line integral reaction path approximation for large systems via nonlinear constrained optimization: Application to alanine dipeptide and the  \$\beta\$  hairpin of protein G](#)  
*J. Chem. Phys.* **124**, 194903 (2006); 10.1063/1.2194544

[Dynamic coupling between coordinates in a model for biomolecular isomerization](#)  
*J. Chem. Phys.* **124**, 144911 (2006); 10.1063/1.2183768

[Inclusion of quantum-mechanical vibrational energy in reactive potentials of mean force](#)  
*J. Chem. Phys.* **114**, 9953 (2001); 10.1063/1.1371497

---



**NEW Special Topic Sections**

**NOW ONLINE**  
Lithium Niobate Properties and Applications:  
Reviews of Emerging Trends

**AIP** | Applied Physics  
Reviews

# Reproducing kernel potential energy surfaces in biomolecular simulations: Nitric oxide binding to myoglobin

Maksym Soloviov and Markus Meuwly<sup>a)</sup>

Department of Chemistry, University of Basel, Klingelbergstrasse 80, 4056 Basel, Switzerland

(Received 7 April 2015; accepted 9 July 2015; published online 10 September 2015)

Multidimensional potential energy surfaces based on reproducing kernel-interpolation are employed to explore the energetics and dynamics of free and bound nitric oxide in myoglobin (Mb). Combining a force field description for the majority of degrees of freedom and the higher-accuracy representation for the NO ligand and the Fe out-of-plane motion allows for a simulation approach akin to a mixed quantum mechanics/molecular mechanics treatment. However, the kernel-representation can be evaluated at conventional force-field speed. With the explicit inclusion of the Fe-out-of-plane (Fe-oop) coordinate, the dynamics and structural equilibrium after photodissociation of the ligand are correctly described compared to experiment. Experimentally, the Fe-oop coordinate plays an important role for the ligand dynamics. This is also found here where the isomerization dynamics between the Fe–ON and Fe–NO state is significantly affected whether or not this co-ordinate is explicitly included. Although the Fe–ON conformation is metastable when considering only the bound  $^2A$  state, it may disappear once the  $^4A$  state is included. This explains the absence of the Fe–ON state in previous experimental investigations of MbNO. © 2015 AIP Publishing LLC. [<http://dx.doi.org/10.1063/1.4929527>]

## I. INTRODUCTION

Following the dynamics of small ligands in (globular) proteins provides information about the internal structure of the macromolecule and about the way how ligand and protein motions are coupled. By combining experimentation and simulation, a detailed picture about these processes can be obtained. One of the paradigmatic systems in this context is myoglobin (Mb) and its ligands O<sub>2</sub>, CO, or nitric oxide (NO), see Figure 1. NO is a key messenger for many biological processes in vertebrates. It can bind to Mb, and together with O<sub>2</sub> can be catalyzed by Mb to form nitrate.<sup>1</sup> The rebinding kinetics of NO to Mb has been studied intensively over the past three decades using experimental and computational methods.<sup>2–14</sup> Compared to rebinding of CO, no substantial rebinding barrier has been found for geminate recombination of NO to the heme Fe<sup>3+</sup> and *ab initio* calculations have even suggested that the recombination reaction may be barrierless for NO in specific conformations.<sup>15</sup> Because of the short time scale involved (picoseconds), this process is ideally suited to be investigated computationally at an atomistic level.<sup>10–14</sup>

Over the past few years, computational investigations of ligand migration in globular proteins have provided considerable insights into their structure, energetics, and dynamics.<sup>16–19</sup> All these efforts require adequate representations of the intermolecular interactions. Methods for this range from purely empirical force fields to mixed quantum mechanical/molecular mechanics (QM/MM) treatments. They all have their merits and disadvantages in terms of computational efficiency and realism in capturing the essentials of the interactions. While

empirical force fields are fast in terms of evaluating the energies and forces of a given configuration, they need to be fitted to a parametrized form, their accuracy is limited and they do not allow to describe bond-breaking and bond-forming processes. On the other hand, mixed QM/MM simulations can be more accurate depending on the level of theory used in the quantum part, but their application is usually limited to single (or few) trajectory of short duration.<sup>20,21</sup> In particular for systems containing metal atoms—as is the case in Mb where the active site is the Fe-heme unit—even density functional theory (DFT)-based approaches become computationally challenging. Furthermore, technical difficulties can arise, e.g., converging the Hartree Fock wavefunction or maintaining the correct electronic state, if sufficiently distorted conformations are sampled in the molecular dynamics (MD) simulations.

An alternative to QM/MM is to explicitly parametrize the total energy (instead of representing the total energy as sum over individual force field terms) for a subsystem based on rigorous quantum chemistry and combine this with an empirical force field. Again, the parametrization step is critical and often time-consuming. Such an approach has, for example, been used in combining accurate representations for the proton transfer energetics between a donor atom and an acceptor atom together with empirical force field parameters for the environment.<sup>22</sup> The approach—molecular mechanics with proton transfer (MMPT)—has been successful to realistically follow the proton transfer dynamics in protonated water dimer, diglyme, malonaldehyde, or even in a metal-catalyst used for hydroformylation.<sup>23–25</sup> However, because the quantum-based energies cannot always be represented by standard harmonic terms in order to take full advantage of their higher accuracy, tedious non-linear fits are often involved in

<sup>a)</sup> Author to whom correspondence should be addressed. Electronic mail: [m.meuwly@unibas.ch](mailto:m.meuwly@unibas.ch)

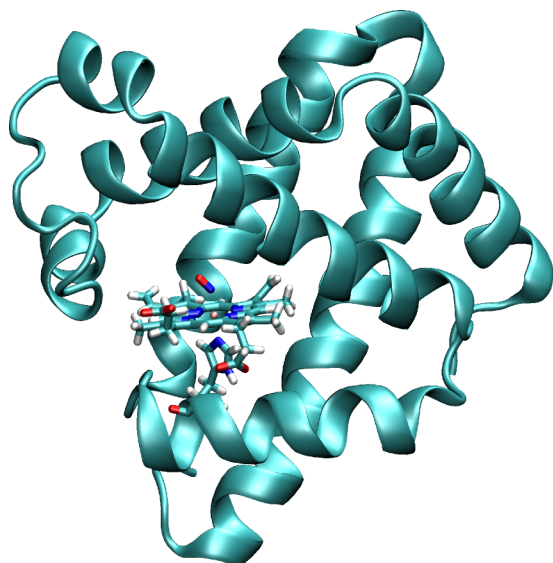


FIG. 1. NO-bound myoglobin with the heme, His93, and NO ligand in licorice and the protein in secondary structure representation.

the parametrization. In the present work, reproducing kernel interpolation will be used instead of carrying out a (non-)linear least squares fit.

Recent experiments have followed the interplay between the Fe-out-of-plane (Fe-oop) and the NO-ligand motion in a time resolved fashion.<sup>7</sup> This work points towards a direct coupling between these degrees of freedom on the 10 to 100 ps time scale. Running a statistically significant number of QM/MM trajectories from which to analyze and atomistically resolve the interplay of the motions involved is beyond current computational methods. In order to retain the accuracy needed, the total interaction in the protein-ligand system is decomposed in a similar fashion and the subsystem—ligand and Fe-oop coordinate—is treated at the DFT level. Subsequently, a suitable representation that preserves the accuracy of the interpolated potential energy surface (PES) is chosen and used in the simulations. An alternative to parametrized representations of PESs is parameter-free, reproducing kernel Hilbert space (RKHS)-based representations of reference data from quantum chemical calculations.<sup>26,27</sup> They are based on smoothness criteria of the interpolant and have been successfully applied to study van der Waals complexes<sup>28,29</sup> and reactions.<sup>30,31</sup> One of the hallmarks of an RKHS-interpolated PES is that it reproduces the reference energies *exactly* (i.e., by construction) which is not the case for parametrized force fields.

In the present work, RKHS-based representations for a subsystem for which accurate energetics is required are combined with a force field description of the protein environment. The subsystem contains the ligand (nitric oxide) degrees of freedom and the heme Fe-oop motion which has been shown to be decisive for the two limiting states (bound and unbound) and the dynamics between them. The interpolated PESs are then used to explore the ligand dynamics in the  $^2A$  and  $^4A$  states. The approach used in the present work also allows to following the isomerization dynamics of the ligand which involves bond-breaking and bond-formation between the heme

Fe and the ligand. First, the computational models are presented. Next, the RKHS-PES is discussed and its performance in atomistic simulations is assessed. Finally, the dynamics on the two electronic states of interest is characterized and compared with experiment and previous work.

## II. METHODS

### A. Intermolecular interactions

The total potential energy of the system  $V_{\text{tot}}(\vec{X})$ , where  $\vec{X}$  is the position vector for all  $N$  atoms, is written as

$$V_{\text{tot}}(\vec{X}) = V_{\text{FF}}(\vec{Q}) + V(R, \theta, \phi). \quad (1)$$

Here,  $V_{\text{FF}}(\vec{Q})$  is the standard CHARMM22 force field,<sup>32</sup> which is employed for all the coordinates of the configuration space  $\vec{Q}$  except  $(R, \theta, \phi)$ , which are the coordinates describing the interactions between the heme-Fe and NO, and the doming coordinate of the heme-Fe. The doming coordinate describes the transition between an in- and out-of-plane iron atom upon changing its ligation state from 6- to 5-coordinated (ligand bound to ligand unbound, see Figure 2). The nitric oxide ligand is described by a harmonic bond with force constants of 824.93 and 1101.46 kcal/mol to reflect the changing strength in the NO bond upon binding and unbinding.<sup>12</sup> The  $R$  coordinate is the distance between the heme Fe and the geometrical center of NO,  $\theta$  is the angle between  $R$  and the NO-molecular axis, and  $\phi$  is the average angle between each of the four heme-nitrogen atoms, the heme-Fe, and the  $N_{\epsilon}$  of the axial His93. Therefore,  $\theta$  describes the NO rotation and  $\phi$  corresponds to the heme doming.

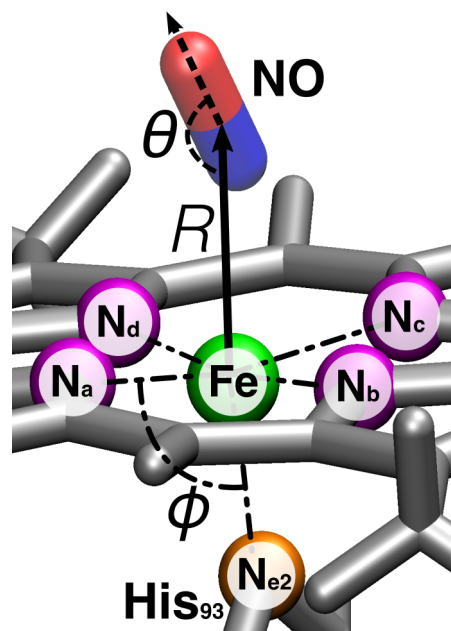


FIG. 2. Relevant coordinates for the energetics of bound NO and unbound NO. Heme-nitrogens  $N_a$  to  $N_d$  (purple) heme-Fe (green),  $N_{\epsilon}$  of His93 (orange), and the N and O atoms of NO molecule are blue and red. The distance between the heme Fe and the center of the NO molecule is  $R$ ,  $\theta$  is the angle between  $R$  and the NO-molecular axis, and  $\phi$  is the average angle between each of the four heme-nitrogen atoms, the heme Fe, and the  $N_{\epsilon}$  of the axial His93.

The reference energies for the 3-dimensional PES  $V(R, \theta, \phi)$  were obtained from DFT calculations based on the B3LYP<sup>33–36</sup> functional together with the 6-31G(d,p) basis set.<sup>37,38</sup> Gaussian09<sup>39</sup> was used to perform all DFT calculations. The model system contains a truncated heme group, the NO ligand and a methyl-imidazole as a core of the axial histidine (His93), see Figure 2. The reference points were calculated on a 3-dimensional grid: The  $R$ -co-ordinate was scanned between 1.7 and 3.9 Å with step size  $\Delta R = 0.1$  Å. The distance  $d$  between the heme-Fe and the heme-plane included positions  $d = 0.2$  and  $0.1$  Å (for the  ${}^4A$  state only) above the plane, the in-plane  $d = 0.0$  Å position, and  $d = -0.1, -0.3,$  and  $-0.5$  Å below the plane. For  $\theta$ , an 11-point Gauss-Legendre grid including angles of  $\theta[^\circ] = 11.815, 27.452, 43.089, 58.726, 74.363, 90.000, 105.637, 121.274, 136.911, 152.548,$  and  $168.185$  was employed. The out-of-plane distance used in the DFT grid was translated into an average angle  $\phi$  between the heme-nitrogen, heme-Fe, and the  $N_\epsilon$  of the axial histidine ligand via standard trigonometry.

The calculations were carried out for the  ${}^2A$  and  ${}^4A$  states using a 3-dimensional grid resulting in 1210 and 1452 reference points for the two states, respectively. In addition, 100 validation points for both  ${}^2A$  and  ${}^4A$  states were computed at off-grid points for different values of  $r$  and  $\theta = 30^\circ, 60^\circ, 120^\circ$  and  $\phi = 87^\circ, 90^\circ, 92^\circ, 95^\circ$ . The root mean square error for the validation set as determined from the fitted PES was 1.0 kcal/mol and 1.1 kcal/mol for the  ${}^2A$  and  ${}^4A$  PESs, respectively. This is close to chemical accuracy except for errors in the quantum chemical methods used.

Initially, a parametrized fit of the PES was attempted. However, it was found that in particular representing the Fe-ooop coordinate in parametrized form was difficult. Hence, a different approach was considered. Kernel-based representations are a powerful means to *exactly* reproduce the target data while maintaining desirable smoothness and asymptotic behavior of the inter- and extrapolant. The explicit form of the RKHS PES is as follows:

$$V(R, \theta, \phi) = \sum_{\lambda=0}^{10} V_\lambda(R, \phi) P_\lambda(\cos(\theta)) + V_c(\phi), \quad (2)$$

where  $P_\lambda$  are Legendre polynomials and  $V_c$  is a harmonic potential. By construction, the kernel-based part of the potential  $\sum_{\lambda=0}^{10} V_\lambda(R, \phi) P_\lambda(\cos(\theta))$  decays asymptotically ( $R \rightarrow \infty$ ) to zero. The harmonic potential  $V_c$ ,

$$V_c(\phi) = \frac{1}{2} k (\phi - \phi_e)^2, \quad (3)$$

captures the asymptotic energies of the different  $V(R, \theta)$  potential energy surfaces depending on the Fe-ooop position where  $k$  is the force constant, and  $\phi_e$  is the equilibrium position. Both  $k$  and  $\phi_e$  are parametrized during the optimization of the potential  $V(R, \theta, \phi)$ . The final parameters in the  ${}^2A$  state are  $k = 0.165$  kcal/mol and  $\phi_e = 95.6^\circ$  and in the  ${}^4A$  state,  $k = 0.116$  kcal/mol and  $\phi_e = 93.8^\circ$ .

The radial strength functions  $V_\lambda(R, \phi)$  are represented as a reproducing kernel,<sup>26</sup>

$$V_\lambda(R, \phi) = \sum_{i,j} \beta_{\lambda,i,j} \cdot \mathcal{K}(R, R_i) \cdot \mathcal{G}(\phi, \phi_j), \quad (4)$$

where  $\mathcal{K}(R, R_i)$  is a radial reproducing kernel<sup>27,28</sup> and  $\mathcal{G}(\phi, \phi_j)$  is a Gaussian reproducing kernel.<sup>40</sup> The explicit form of the radial reproducing kernels used here is

$$\mathcal{K}(R_i, R_j) = \frac{1}{14} R_{>}^{-7} \left( 1 - \frac{7 R_{<}}{9 R_{>}} \right), \quad (5)$$

where  $R_{>}$  and  $R_{<}$  are the greater distance and smaller distance, respectively, for any pair of  $R$ - values. The Gaussian kernels are parametrized as follows:

$$\mathcal{G}(\phi_i, \phi_j) = \exp\left(-\frac{(\phi_i - \phi_j)^2}{2\sigma^2}\right), \quad (6)$$

where  $\sigma$  is the width of the kernel and its value of  $\sigma = 5^\circ$  was chosen such that the kernels overlap and the optimization result in smallest error on the reference data set. Therefore, kernels are symmetric positive definitive and describe the correct asymptotic behavior at large  $R$  as  $\mathcal{K}$  decays to zero.

The  $\beta_{\lambda,i,j}$  are determined from a singular value decomposition<sup>41–43</sup> for each value of  $\lambda$  and hence are not adjustable fitting parameters as would be the case in a typical non-linear least squares fit.<sup>29</sup> In order to prevent overfitting, Tikhonov regularization (parameter  $\alpha = 10^{-7}$ ) is used<sup>44,45</sup> to penalize solutions of large norm and to stabilize the procedure. The coefficients  $\beta_\lambda$  are found from solving the least-square minimization problem,

$$\begin{aligned} \hat{\beta}_\lambda &= \arg \min_{\beta_\lambda} \{ \|K \beta_\lambda - E_\lambda\|^2 + \alpha \|\beta_\lambda\|^2 \} \\ &= (K^T K + \alpha I)^{-1} K^T E_\lambda. \end{aligned} \quad (7)$$

Here,  $K$  is the kernel matrix and  $E_\lambda$  are the DFT energies. The kernel matrix  $K$  is constructed based on the product kernel  $k_{i,j}$ ,

$$k_{i,j} = \mathcal{K}(R_i, R_j) \mathcal{G}(\phi_i, \phi_j), \quad (8)$$

where  $\mathcal{K}(R_i, R_j)$  and  $\mathcal{G}(\phi_i, \phi_j)$  are the radial and Gaussian kernels, respectively, which are calculated for every single pair of values  $(R_i, \phi_i)$  and  $(R_j, \phi_j)$  of the grid.

In addition, for molecular dynamics simulations, forces are required. The necessary derivatives of the RKHS PES can be obtained analytically which yields good energy conservation in *NVE* simulations.

## B. Molecular dynamics simulations

The kernel-based interpolation was implemented into the CHARMM program<sup>46</sup> which was used for all MD simulations together with the CHARMM22 force field.<sup>47</sup> The protein was set up as described previously.<sup>12,48</sup> Mb contains 153 amino acid residues, a heme group, and a nitrogen oxide molecule. Simulations were carried out for both, His<sub>86</sub>64 and His<sub>64</sub>64 protonation, with the latter being the more likely state.<sup>49–53</sup> Contrary to the previous work which employed stochastic boundaries, in the present work, the protein was solvated in a periodic, pre equilibrated waterbox  $62.0864 \times 62.0864 \times 62.0864$  Å<sup>3</sup>. The final system contains 23 711 atoms. All bonds involving hydrogens were treated using SHAKE<sup>54,55</sup> with a tolerance of  $10^{-6}$ . For the non-bonded interactions a cutoff of 14 Å was used. First, the system was minimized using steepest-descent and adopted basis Newton-Raphson algorithms. Then, it was heated from 100 to 300 K during 60 ps and equilibrated for

500 ps. This was followed by production runs in the  $NVT$  ensemble as described further below. The time step in all simulations was  $\Delta t = 1$  fs and the velocity Verlet integrator was used to propagate the equations of motion.

### III. RESULTS AND DISCUSSION

#### A. The fitted PES

The results show that the fitted  $^2A$  PES has two well-defined minima, which correspond to the Fe–NO and Fe–ON states. These two states have already been found in earlier work<sup>48,56</sup> but are absent in other investigations.<sup>57</sup> Previous work found an energy difference of 15.3 kcal/mol between the two states whereas the present B3LYP/6-31G\*\* calculations yield 18.1 kcal/mol. In order to confirm their existence, additional electronic structure calculations were carried out. For this, the Fe–NO and Fe–ON structures were separately optimized at the UB3PW91/6-31G\*\* level of theory. The converged energies differ by 18.5 kcal/mol and establish that both conformational isomers also exist with this functional. Experimentally, the existence of an Fe–ON state has been found for model systems,<sup>56,58,59</sup> but not for NO in Mb.<sup>60</sup>

The NO-binding energy on the  $^2A$  PES is 23.7 kcal/mol, see Figures 3 and 4. Figure 3 illustrates that the RKHS-PES exactly matches the reference DFT-points. Also, it can be seen that the binding energy of the ligand depends on the Fe–oop position and that upon NO-dissociation from an in-plane position, the asymptotic energy is higher than for dissociation from an out-of-plane position. At infinite separation of the NO from the heme-Fe (see Figure 2), the Fe atom moves 0.2 Å below the porphyrin plane ( $d = -0.2$  Å) and correctly predicts the doming effect. The experimentally observed out-of-plane distance in the high-resolution X-ray structure of Mb<sup>61</sup> is  $-0.25$  Å and the one found in the previous work is  $-0.35$  Å.<sup>12</sup> The out-of-plane positioning of the heme-Fe in the model system and in the protein differs because the protein environment exerts forces which affect the equilibrium

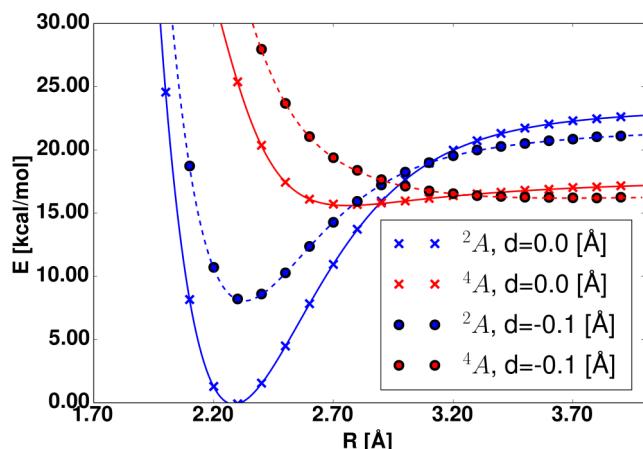


FIG. 3. Radial cuts through the PES for  $\theta = 152.06^\circ$  and different out-of-plane displacements (shown in the legend). Symbols represent the reference DFT points; solid and dashed lines are the RKHS PES. When the NO molecule dissociates from an in-plane position (crosses) the asymptotic energy is higher than for dissociation from an out-of-plane position (circles). The binding energies of the ligand also depend on the Fe–oop position.

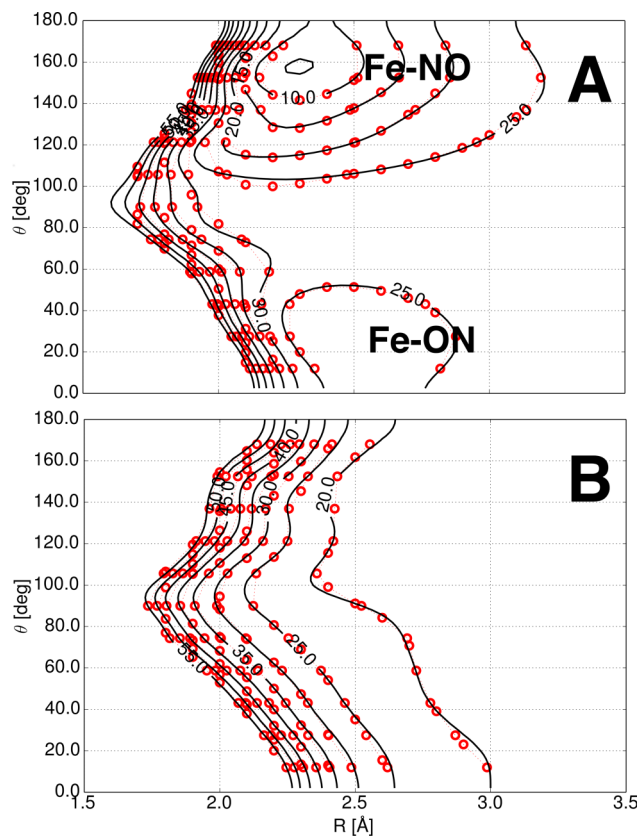


FIG. 4. PESs for the two states considered here. Black isocontours are the RKHS-PES and red circles are the DFT reference points for the Fe-in-plane conformation ( $\phi = 90^\circ$ ). (a) The Fe–NO bound state,  $^2A$ , with the global minimum in a bent Fe–NO conformation, the secondary minimum (Fe–ON) 20.2 kcal/mol, and the transition state separating the two states at 23.7 kcal/mol above the global minimum. (b) The unbound,  $^4A$ , state. The energies of this state are close to those of the  $^2A$  state around the Fe–ON conformation which may wash out this secondary minimum.

structure. This can be taken into account by the harmonic angular potential ( $N_{\text{heme}}\text{–Fe–}N_{\text{His}}$ ) of the force field. The  $^4A$  state does not have a clear minimum energy structure, see Figure 4, and mostly represents a van der Waals complex with an equilibrium Fe–CoM<sub>NO</sub> distance of 3.5 Å.

#### B. Validation simulations

In order to validate the implementation of the total potential energy function—and the RKHS-interpolation in particular—and the corresponding derivatives, several  $NVE$  simulations 500 ps in length were carried out. The average fluctuation of  $p(E - \langle E \rangle)$  is 1 kcal/mol for simulations with the kernel-based PESs for the  $^2A$  and  $^4A$  states. As a comparison, simulations for the  $^2A$  state were run using the force field parameters from previous work<sup>12</sup> and showed identical results. Also, no drift in the total energy is found. This validates the present implementation of the kernel-based PES.

It is also of interest to compare the results from simulations with and without the RKHS potential. A meaningful target is the dynamics of the Fe–oop motion which is functionally relevant and has also been investigated spectroscopically.<sup>72</sup> After breaking the Fe–NO bond, the Fe immediately starts to move below the heme-plane on a  $\sim 100$  fs time

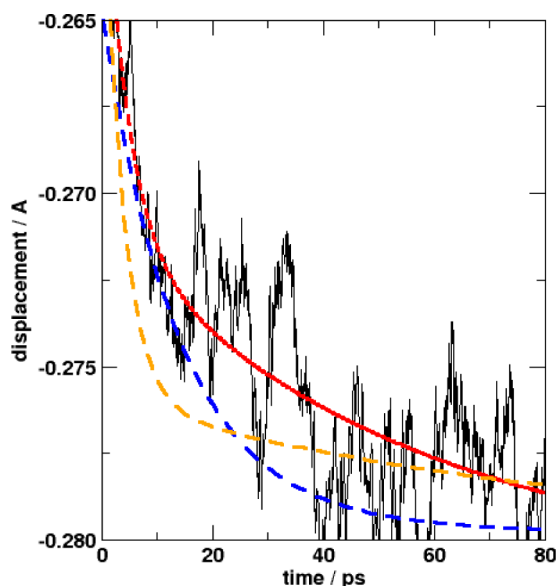


FIG. 5. Averaged time dependence over a 2 ps sliding window of the Fe-oop motion after photodissociation of the ligand and subsequent dynamics on the “FF plus RKHS”  $^4A$  PES. The ultrafast, sub-picosecond component is averaged out and not visible and the raw data (black trace) are shown together with the overall fit (red trace). The experimentally determined spectral shifts (orange) and the relaxation dynamics from the “FF only” simulations (blue) were scaled to superimpose on the results from the “FF plus RKHS” relaxation dynamics.

scale. This is consistent with optical experiments and previous MD simulations.<sup>72,73</sup> Simulations were run with the “FF plus RKHS” potential as in Eq. (1) and with the conventional “FF only.” The same number of runs, carried out under identical conditions, was analyzed in both cases. Using the FF plus RKHS-PES, the simulations yield an overall relaxation dynamics of the Fe-oop position onto which a characteristic beating pattern (see black trace in Figure 5) is superimposed which suggests complex structural changes in the protein. The decay can be fit to a double exponential  $ae^{-t/\tau_1} + be^{-t/\tau_2} + c$  and yields  $\tau_1 = 3.5$  ps and  $\tau_2 = 64.4$  ps, as shown in Figure 5. With the conventional FF only, the dynamics is single exponential (blue trace in Figure 5, with suitably scaled amplitude for direct comparison) with a time constant of  $\tau_1 = 13.7$  ps. Optical experiments also find two time constants: 3.5 ps and 83.0 ps for the two processes on the picosecond time scale, respectively (orange trace).<sup>72</sup> The numerical values are summarized in Table I and suggest that the FF plus RKHS potential energy surface faithfully captures the existence and magnitude of two time constants whereas the conventional FF does not. On the other hand, the relative amplitudes  $a_1 : a_2$  of the fast and slow

TABLE I. Parameters of the double exponential fits to the data. The units for the amplitudes  $a_1$  and  $a_2$  are Å for the simulations and  $\text{cm}^{-1}$  for the experiments.<sup>72</sup> Parameter  $b$  reports on the equilibrium Fe-oop position and the experimental value is from Ref. 61.

	$\tau_1$ (ps)	$\tau_2$ (ps)	$a_1$ (Å or $\text{cm}^{-1}$ )	$a_2$ (Å or $\text{cm}^{-1}$ )	$b$ (Å)
FF only	13.7		0.025		-0.43
FF + RKHS	3.5	64.4	0.012	0.010	-0.28
Experiment <sup>61,72</sup>	3.5	83.0	85.0	19.0	-0.25

process differ between experiment ( $\approx 4 : 1$  for fast vs. slow) and the FF plus RKHS simulations ( $\approx 1 : 1$ ), as can also be seen in Figure 5. This is, however, not surprising, as the physical process probed is not exactly the same. The experiment reports on the temporal decay of a change in the electronic structure around the heme group which leads to ligand dissociation and structural dynamics whereas the atomistic simulations only follow the structural relaxation following bond breaking.

This structural dynamics has also been investigated from earlier simulations with a somewhat different computational setup but the same force field for the heme-group. Most importantly, a constant dielectric was used<sup>3,73</sup> in the earlier simulations whereas in the present case, the water solvent was treated explicitly. These earlier simulations found two time scales with amplitudes of the fast and slow processes close to each other ( $1 : 1$ ), as was also found for the FF plus RKHS simulations described above. Unfortunately, a typo in the sign of one of the decay times must have occurred which prevents explicit comparison. The current work leads to an Fe-oop distance of  $\approx -0.28$  Å which compares well with the experimentally measured result ( $-0.25$  Å)<sup>61</sup> contrary to earlier simulations ( $-0.60$  Å).<sup>73</sup> Hence, the FF plus RKHS simulations find two time scales for the structural relaxation of the Fe-oop motion with about equal amplitude of the two processes and an equilibrium value ( $-0.28$  Å) for the Fe-oop position in agreement with experiments ( $-0.25$  Å). This is not the case for the FF-only simulations (which find  $-0.43$  Å) carried out under identical conditions, see Figure 5 and comparison in Table I.

To further compare results from simulations using the current RKHS-PES with existing data,<sup>48</sup> the Fe-ON  $\rightarrow$  Fe-NO isomerization dynamics was studied on the 2-dimensional surface, i.e., for  $\phi = 90^\circ$ . For this, 250 trajectories were initiated from the Fe-ON local minimum energy structure. The kinetic curves (see Figure 6(a)) were determined from trajectories which lead to isomerization within 250 ps. The ensuing isomerization kinetics are the blue and magenta traces in Figure 6(a) for His<sub>64</sub> and His<sub>e64</sub> protonation, respectively. For the kinetic curves, isomerization was considered to occur if the NO coordinates fulfill the criterion ( $R = 2.55$  Å and  $\theta = 130^\circ$ ). The typical isomerization time is on the 100 ps time scale. This is in qualitative agreement with previous crossing times which ranged from 50 ps to 600 ps<sup>48</sup> using about 10 trajectories, from which, however, no rigorous distribution of the crossing times could be determined. The 100 ps found here qualitatively agree with the earlier work and the shorter isomerization times found here are explained by the lower barrier in the present PES. It is concluded that the two different PES parametrizations (Morse plus Legendre versus RKHS-plus-Legendre here) yield qualitatively similar isomerization times with the present simulations exhibiting more rapid dynamics due to the lower isomerization barrier. Also, the difference between the two protonation states of His<sub>64</sub> are small; the yield within 250 ps differs by about 10%.

### C. Equilibrium dynamics of the $^2A$ and $^4A$ states

The well depth of the bound Fe-NO minimum is 23.7 kcal/mol. In the  $^2A$  state, the conformationally averaged

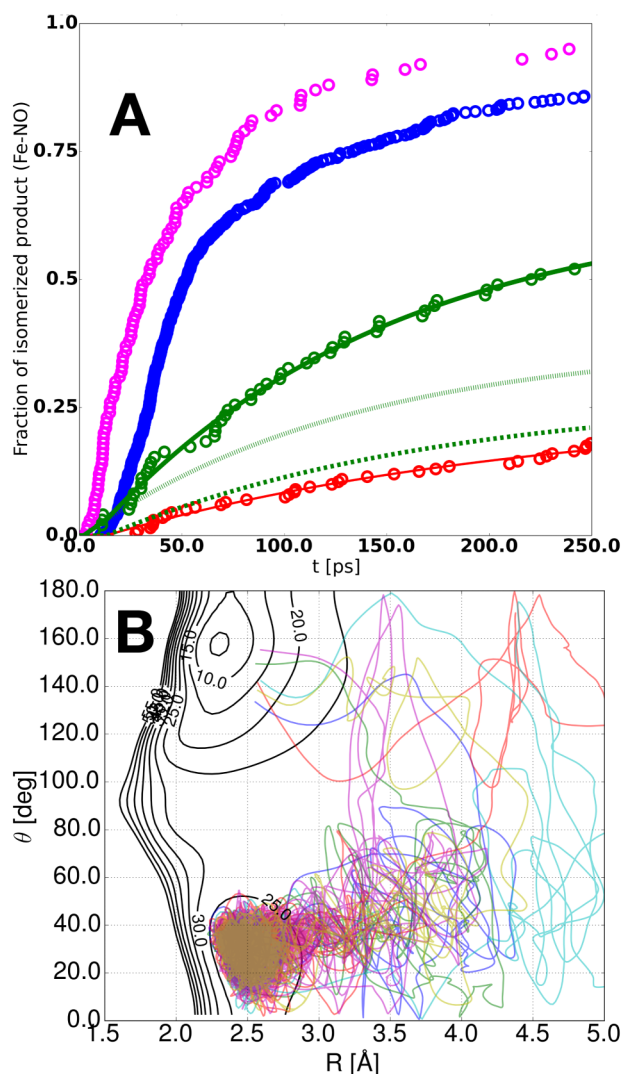


FIG. 6. (a) NO isomerization kinetics (fraction of product formed as a function of time) on the  $^2A$  PES with (3D—red and green for His $_{\delta}$ 64 and His $_{\epsilon}$ 64 protonation, respectively) and without (2D—blue and magenta for His $_{\delta}$ 64 and His $_{\epsilon}$ 64 protonation, respectively) explicitly taking into account the Fe-ooP coordinate. Fits to single and double exponentials (see text) are in solid lines. The short (dashed green) and long (dotted green) components describe the two processes found for His $_{\delta}$ 64 protonation. (b) Projections of several representative trajectories for the Fe-ON  $\rightarrow$  Fe-NO isomerization dynamics on the 3-dimensional PES including the Fe-ooP motion, superimposed on the  $^2A$  PES. The Fe-ON state has  $\theta = 30^\circ$  whereas the Fe-NO state is characterized by  $\theta = 150^\circ$ .

Fe-N distance is  $1.79 \pm 0.04$  Å and the average Fe-N-O angle is  $147.5 \pm 4.6^\circ$ . These values are in good agreement with the experimentally determined structures with nitric oxide bound to the heme-Fe, including myoglobin,<sup>62–64</sup> indoleamine

2,3-dioxygenase,<sup>65</sup> cytochrome c oxidase,<sup>66</sup> and others (see Table II). The differences might be explained by the effects of the crystal field and the specific structure and electrostatic environment of the distal pocket.

The motion of the NO molecule is significantly affected by the structure of the active site, especially by the His64 residue. One important determinant in the photodissociation process is the local structure surrounding the bound ligand at the moment of excitation. This is largely determined by the positioning of the His64 side chain. The significant lowering in the probability of the dihedral angle  $\phi_1 = (\text{N}_a\text{-Fe-N-O})$  in Figure 7(a) is caused by excluded volume not easily accessible to the bound ligand due to the proximity of His64 and differs for the two protonation states His $_{\delta}$ 64 and His $_{\epsilon}$ 64. For His $_{\delta}$ 64, one low-probability state exists (at  $\approx 60^\circ$ ) whereas for His $_{\epsilon}$ 64, there are two, see Figure 7(a). The minima at  $\phi_1 \approx 60^\circ$  coincide whereas that at  $\phi_1 \approx -90^\circ$  only occur for His $_{\epsilon}$ 64. Further analysis of the trajectories suggests that for His $_{\epsilon}$ 64, the side chain can occupy two distinct states (see Figure 7(b)) whereas there is only one conformation for His $_{\delta}$ 64.

Although the Fe-ON state has not been characterized experimentally so far in MbNO, considering the ground state  $^2A$  dynamics is still valuable for several reasons. First, it allows to assess the coupling between the ligand motion and the Fe-ooP dynamics and second, direct comparison with previous simulations at a considerably lower level of theory is possible (see Sec. III B). Finally, when rebinding from the  $^4A$  state, the NO-ligand crosses to the  $^2A$  state in a large range of geometries and hence, exploration and characterization of the full  $^2A$  PES are meaningful and relevant.

Previously, the motion of bound NO has been investigated on a fitted, parametrized two-dimensional PES based on B3LYP//VDZ/3-21G calculations.<sup>48</sup> This PES was parametrized for the in-plane position of Fe; therefore,  $\phi = 90^\circ$  throughout. As a first step, the performance of the present PES, which relies on a RKHS representation, is compared to simulations on the earlier Legendre expansions with Morse functions for the radial coordinate. As it was already mentioned, the  $^2A$  state has two well defined minima (Fe-NO and Fe-ON). The isomerisation barrier for Fe-NO  $\rightarrow$  Fe-ON is 23.7 (21.4 previous work) kcal/mol, whereas the barrier for the reverse reaction is around 3.5 kcal/mol (8.4 kcal/mol in previous work).<sup>48</sup> Part of these differences are due to the considerably larger basis set used in the present work.

Compared to simulations on the 2D-PES, following the dynamics on the 3D-PES explicitly including the Fe-ooP motion shows that within the maximum simulation time of 250 ps, a considerably smaller number of trajectories completes the conformational transition between Fe-ON and Fe-NO, see

TABLE II. Characteristic bond lengths and angles for the active site of MbNO obtained from X-ray structures of NO-bound myoglobins and related heme-containing proteins and the present simulations.

Reference	Fe-N (Å)	Fe-N-O (deg)	Structure resolution (Å)
Mb (MD, current work)	$1.79 \pm 0.04$	$147.46 \pm 4.60$	...
Horse heart Mb <sup>67</sup>	1.87	144	1.3
Sperm whale myoglobin (1HJT) <sup>62</sup>	1.89	112	1.7
Horse heart (MS XAFS) <sup>68</sup>	1.75	150	...

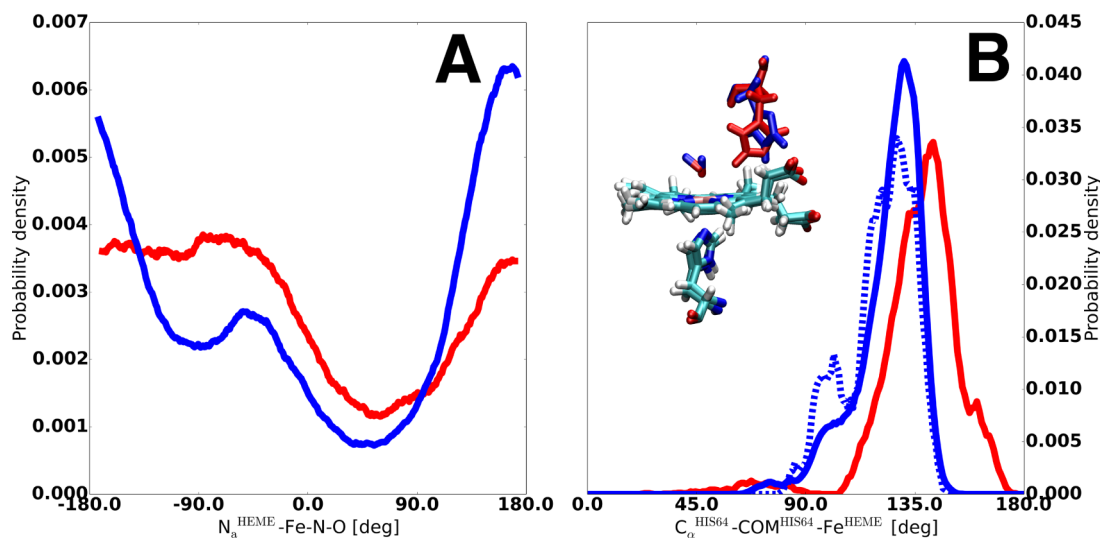


FIG. 7. (a) The probability distribution for the  $N_{\alpha}$ -Fe-N-O dihedral angle  $\phi_1$  (see Figure 1) characterizing the orientation of heme-bound NO with His $_{\delta}$ 64 (red) and His $_{\epsilon}$ 64 (blue). For His $_{\delta}$ 64, one prominent orientation is observed whereas for His $_{\epsilon}$ 64, there are two. (b) The averaged  $\phi_2 = C_{\alpha}^{\text{His64}}\text{-CoM}^{\text{His64}}\text{-Fe}$  angle distribution for the two protonation states. The shoulder at  $\phi_2 = 100^\circ$  for His $_{\epsilon}$ 64 corresponds to the second state ( $\phi_1 = -90^\circ$ ) in panel (a) (and the blue orientation in the inset) and is typically occupied for tens of picoseconds during the simulations. The blue dashed line is from a single trajectory in which the two states are more clearly separated.

red and green traces in Figure 6(a). Compared to  $\approx 80\%$  (His $_{\delta}$ 64) and  $95\%$  (His $_{\epsilon}$ 64) on the 2-dimensional PES, only  $\approx 25\%$  (His $_{\delta}$ 64) and  $50\%$  (His $_{\epsilon}$ 64) isomerize when running the simulations on the 3-dimensional PES including the Fe-oop coordinate. This suggests that once the NO ligand rebinds to the  $^2A$  state coming from the  $^4A$  state, its dynamics is strongly coupled to the Fe-oop motion. It is evident that not only a smaller fraction of trajectories leads to isomerization but also the kinetics is also slowed down compared to the 2D-simulations in which the Fe-oop coordinate is not explicitly included and the iron is always in an in-plane position, available to bond-formation.

Figure 6(b) shows representative isomerization trajectories for His $_{\delta}$ 64 leading to Fe-NO using the 3D potential. First, the Fe-O bond is broken and the NO molecule leaves in the configuration, which is similar to the initial Fe-ON minimum. Then, being affected by the protein active site, the ligand rotates and rebinds to the heme-Fe in the thermodynamically favoured Fe-NO configuration. Depending on the detailed dynamics such a transition lasts up to 10 ps, see Figure 8. When leaving the Fe-ON minimum, the heme-Fe moves below the heme-plane, making it more difficult to be accessed by the NO molecule when forming the Fe-NO bond compared to the situation when the Fe-oop co-ordinate is not explicitly included in the PES.

The isomerization rates using the 3D-PES for His $_{\delta}$ 64 in Figure 6(a) (red trace) can be fit to a single exponential  $1 + a_1(e^{-(t-\tau_1)/t_1} - 1)$ , where  $\tau_1 = 12.7$  ps is the lag time,  $t_1 = 215$  ps is the characteristic time, and  $a_1 = 0.25$  is the amplitude. The lag time corresponds to the shortest transition time in the data set. For His $_{\epsilon}$ 64, a fit involving two exponential processes is required which results in  $\tau_1 = 2.0$  ps,  $t_1 = 131$  ps, and  $a_1 = 0.38$  for the short component and  $\tau_2 = 13.1$  ps,  $t_2 = 163$  ps, and  $a_2 = 0.28$  for the long component. It is noted that the long component (dotted green line) for His $_{\epsilon}$ 64 is almost a fit to the raw data for the isomerization with His $_{\delta}$ 64

(red dots). This suggests that they probe the same conformational substrate ( $\phi_1 = 60^\circ$  in Figure 7). This is further supported by  $\tau_1^{\text{His}_{\delta}} \approx \tau_2^{\text{His}_{\epsilon}}$ . Hence, the rapid process, which only appears for His $_{\epsilon}$ 64, corresponds to the alternative orientation  $\phi_1 = -90^\circ$  in Figure 7(a).

As already mentioned, the existence of the Fe-ON metastable state has been established for heme-model systems but not for NO in Mb. Evidently, the PES does support such a state but whether or not it can be observed experimentally also depends on the energetic ordering of the  $^2A$  and  $^4A$  states.

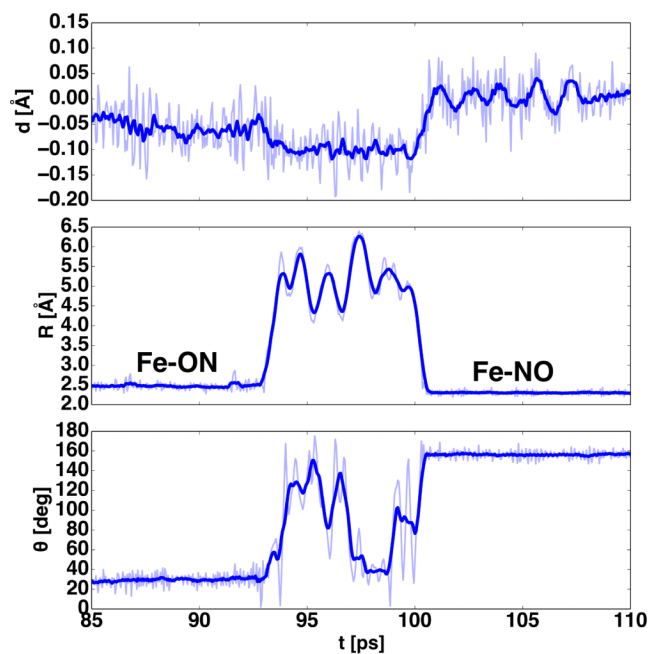


FIG. 8. One Fe-ON  $\rightarrow$  Fe-NO isomerization trajectory highlighting the coupling between ligand and Fe-oop motion. During the time the ligand samples regions away from the heme-Fe, the iron atom moves below the heme plane (between 95 and 100 ps).

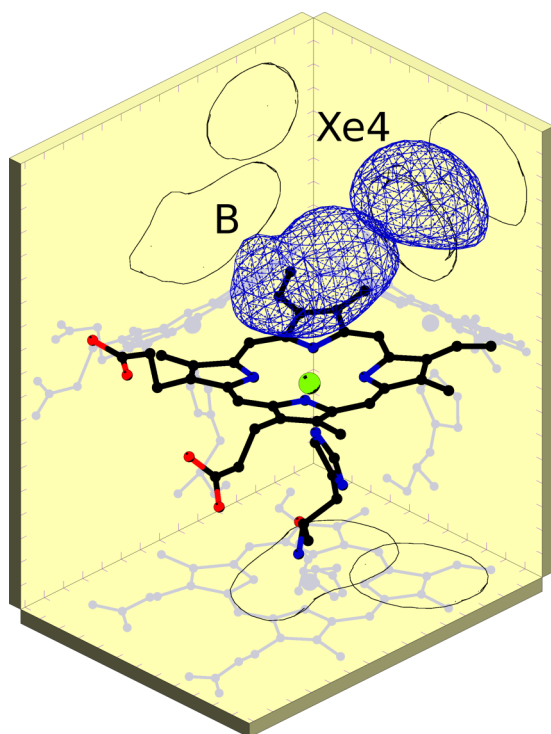


FIG. 9. Effective volume accessed by the NO molecule in the  $^4A$  state. It includes the B and Xe4 states.

Asymptotically, the two states are separated by  $\approx 5$  kcal/mol (see Figure 3) which is close to the stabilization of the Fe–ON minimum relative to the transition state separating it from the Fe–NO state. Furthermore, the protein environment also modulates the energetics of the two electronic states. Taken together, although the DFT calculations establish that the Fe–ON state is a local minimum, observing it in MbNO depends on a delicate balance between the energetics and response to environmental effects of the  $^2A$  and  $^4A$  PESs. The present data suggest that a Fe–NO state has not been found in experiments on MbNO because the  $^4A$  state is lower in energy in this region of phase space, see also Figure 4. Nevertheless, depending on the active-site electrostatics, this may be different for mutated myoglobins or other proteins of the globin family because the energy differences between the electronic states involved are small.

The  $^4A$  photodissociated state is characterized from 50 trajectories, each 500 ps in length. The initial configuration of the system was taken from the  $^2A$  state simulations with an instantaneous excitation by switching the effective PES to the one of the  $^4A$  states. This leads to rapid motion of the NO molecule away from the heme-Fe and consequently diffuse to neighboring protein cavities. The regions accessed by the free NO ligand are illustrated in Figure 9 and include the B state and the Xe4 pocket. These sites match well with the Xe ligand binding pockets found in the X-ray experiments and in previous simulations.<sup>69–71</sup>

#### IV. SUMMARY AND OUTLOOK

The present work introduces kernel-based PESs into atomistic simulations of biomolecular systems. Specifically, it is

possible to carry out simulations at DFT-quality for chemically challenging systems, such as metal centers in proteins, at the speed of regular force fields. For this, the energies of the embedded model system (here heme-His-NO) are precalculated with quantum chemistry and the PES of the relevant coordinates is represented as a RKHS. The implementation yields energy conservation comparable to that of a usual force field. Generalization to more degrees of freedom will require additional technical developments<sup>74,75</sup> also because the number of reference energies scales exponentially when more degrees of freedom are included. However, extensions to 4 or 5 active degrees of freedom are readily possible.

For NO in Mb, the present work clearly shows that including the Fe–oop coordinate has a profound influence on the ligand’s active-site dynamics. This will be of particular interest in better characterizing the rebinding dynamics of photolyzed NO for which recent experimental work suggested the existence of a NO-bound-like, Fe-out-of-plane metastable state.<sup>7</sup> Reactive molecular dynamics simulations<sup>76,77</sup> involving the present  $^2A$  and  $^4A$  kernel-based PESs will provide the necessary information for an atomistically resolved picture linking experiment and molecular dynamics.

#### ACKNOWLEDGMENTS

This work was supported by the Swiss National Science Foundation through Grant Nos. 200021-117810 and the NCCR MUST.

- <sup>1</sup>H. Frauenfelder, B. H. McMahon, R. H. Austin, K. Chu, and J. T. Groves, *Proc. Natl. Acad. Sci. U. S. A.* **98**, 2370–2374 (2001).
- <sup>2</sup>P. Corneliuss, R. Hochstrasser, and A. Steele, *J. Mol. Biol.* **163**, 119–128 (1983).
- <sup>3</sup>J. W. Petrich, J. C. Lambry, K. Kuczera, M. Karplus, C. Poyart, and J. L. Martin, *Biochemistry* **30**, 3975–3987 (1991).
- <sup>4</sup>Q. Gibson, R. Regan, R. Elber, J. Olson, and T. Carver, *J. Biol. Chem.* **267**, 22022–22034 (1992).
- <sup>5</sup>M. Ikeda-Saito, Y. Dou, T. Yonetani, J. Olson, T. Li, R. Regan, and Q. Gibson, *J. Biol. Chem.* **268**, 6855–6857 (1993).
- <sup>6</sup>D. Ionascu, F. Gruia, X. Ye, A. Yu, F. Rosca, C. B. A. Demidov, J. S. Olson, and P. M. Champion, *J. Am. Chem. Soc.* **127**, 16921–16934 (2005).
- <sup>7</sup>S. G. Kruglik, B.-K. Yoo, S. Franzen, M. H. Vos, J.-L. Martin, and M. Negrerie, *Proc. Natl. Acad. Sci. U. S. A.* **107**, 13678–13683 (2010).
- <sup>8</sup>S. Kim, G. Jin, and M. Lim, *J. Phys. Chem. B* **108**, 20366–20375 (2004).
- <sup>9</sup>S. Kim and M. Lim, *J. Am. Chem. Soc.* **127**, 8908–8909 (2005).
- <sup>10</sup>H. Li, R. Elber, and J. E. Straub, *J. Biol. Chem.* **268**, 17908–17916 (1993).
- <sup>11</sup>O. Schaad, H.-X. Zhou, A. Szabo, W. A. Eaton, and E. R. Henry, *Proc. Natl. Acad. Sci. U. S. A.* **90**, 9547 (1993).
- <sup>12</sup>M. Meuwly, O. M. Becker, R. Stote, and M. Karplus, *Biophys. Chem.* **98**, 183–207 (2002).
- <sup>13</sup>D. R. Nutt and M. Meuwly, *Biophys. J.* **90**, 1191–1201 (2006).
- <sup>14</sup>J. Danielsson and M. Meuwly, *J. Chem. Theory Comput.* **4**, 1083–1093 (2008).
- <sup>15</sup>S. Franzen, *Proc. Natl. Acad. Sci. U. S. A.* **99**, 16754–16759 (2002).
- <sup>16</sup>R. Elber and M. Karplus, *J. Am. Chem. Soc.* **112**, 9161–9175 (1990).
- <sup>17</sup>J. Z. Ruscio, D. Kumar, M. Shukla, M. G. Prisant, T. M. Murali, and A. V. Onufriev, *Proc. Natl. Acad. Sci. U. S. A.* **105**, 9204–9209 (2008).
- <sup>18</sup>C. Bossa, M. Anselmi, D. Roccatano, A. Amadei, B. Vallone, M. Brunori, and A. Di Nola, *Biophys. J.* **86**, 3855–3862 (2004).
- <sup>19</sup>N. Plattner, J. D. Doll, and M. Meuwly, *J. Chem. Phys.* **133**, 044506 (2010).
- <sup>20</sup>M.-E. Moret, I. Tavernelli, and U. Rothlisberger, *J. Phys. Chem. B* **113**, 7737–7744 (2009).
- <sup>21</sup>L. M. Lawson Daku and A. Hauser, *J. Phys. Chem. Lett.* **1**, 1830–1835 (2010).
- <sup>22</sup>S. Lammers, S. Lutz, and M. Meuwly, *J. Comput. Chem.* **29**, 1048 (2007).
- <sup>23</sup>S. Lammers and M. Meuwly, *J. Phys. Chem. A* **111**, 1638 (2007).
- <sup>24</sup>J. Huang, M. Buchowiecki, T. Nagy, J. Vanicek, and M. Meuwly, *Phys. Chem. Chem. Phys.* **16**, 204–211 (2014).

- <sup>25</sup>J. Huang, D. Haeussinger, U. Gellrich, W. Seiche, B. Breit, and M. Meuwly, *J. Phys. Chem. B* **116**, 14406–14415 (2012).
- <sup>26</sup>N. Aronszajn, *Trans. Am. Math. Soc.* **68**, 337 (1950).
- <sup>27</sup>T. Hollebeek, T. S. Ho, and H. Rabitz, *Annu. Rev. Phys. Chem.* **50**, 537 (1999).
- <sup>28</sup>T. S. Ho and H. Rabitz, *J. Chem. Phys.* **104**, 2584 (1996).
- <sup>29</sup>M. Meuwly and J. M. Hutson, *J. Chem. Phys.* **110**, 8338 (1999).
- <sup>30</sup>J. Castro-Palacio, T. Nagy, R. Bemish, and M. Meuwly, *J. Chem. Phys.* **141**, 164319 (2014).
- <sup>31</sup>J. Castro-Palacio, R. Bemish, and M. Meuwly, *J. Chem. Phys.* **142**, 091104 (2015).
- <sup>32</sup>A. D. MacKerell, Jr. *et al.*, *J. Phys. Chem. B* **102**, 3586 (1998).
- <sup>33</sup>A. D. Becke, *J. Chem. Phys.* **98**, 5648 (1993).
- <sup>34</sup>C. Lee, W. Yang, and R. Parr, *Phys. Rev. B* **37**, 785 (1988).
- <sup>35</sup>S. Vosko, L. Wilk, and M. Nusair, *Can. J. Phys.* **58**, 1200 (1980).
- <sup>36</sup>P. Stephens, F. Devlin, C. Chabalowski, and M. Frisch, *J. Chem. Phys.* **98**, 11623 (1994).
- <sup>37</sup>G. Petersson and M. A. Al-Laham, *J. Chem. Phys.* **94**, 6081 (1991).
- <sup>38</sup>G. Petersson, A. Bennett, T. Tensfeldt, M. A. Al-Laham, W. A. Shirley, and J. Mantzaris, *J. Chem. Phys.* **89**, 2193 (1988).
- <sup>39</sup>M. J. Frisch *et al.*, GAUSSIAN 09, Revision A.1, Gaussian, Inc., Wallingford, CT, 2009.
- <sup>40</sup>T. Hangelbroek and A. Ron, *J. Funct. Anal.* **259**, 203 (2010).
- <sup>41</sup>C. Eckart and G. Young, *Psychometrika* **1**, 211 (1936).
- <sup>42</sup>M. R. Hestenes, *J. Soc. Ind. Appl. Math.* **6**, 52 (1958).
- <sup>43</sup>G. H. Golub and W. Kahan, *J. Soc. Ind. Appl. Math. Ser. B Numer. Anal.* **2**, 205 (1965).
- <sup>44</sup>A. N. Tikhonov, *Dokl. Akad. Nauk SSSR* **39**, 195 (1943).
- <sup>45</sup>A. N. Tikhonov, *Dokl. Akad. Nauk SSSR* **151**, 501 (1963).
- <sup>46</sup>B. R. Brooks, C. L. Brooks III, A. D. J. Mackerell, L. Nilsson *et al.*, *J. Comput. Chem.* **30**, 1545 (2009).
- <sup>47</sup>A. J. MacKerell, M. Feig, and C. I. Brooks, *J. Comput. Chem.* **25**, 1400 (2004).
- <sup>48</sup>D. R. Nutt, M. Karplus, and M. Meuwly, *J. Phys. Chem. B* **109**, 21118 (2005).
- <sup>49</sup>J. Johnson, D. Lamb, H. Frauenfelder, J. Muller, B. McMahon, G. Nienhaus, and R. D. Young, *Biophys. J.* **71**, 1563–1573 (1996).
- <sup>50</sup>C. Rovira, B. Schulze, M. Eichinger, J. D. Evanseck, and M. Parrinello, *Biophys. J.* **81**, 435–445 (2001).
- <sup>51</sup>K. A. Merchant, W. G. Noid, D. E. Thompson, R. Akiyama, R. F. Loring, and M. D. Fayer, *J. Phys. Chem. B* **107**, 4–7 (2003).
- <sup>52</sup>M. Meuwly, *ChemPhysChem* **7**, 2061–2063 (2006).
- <sup>53</sup>K. Nienhaus, J. S. Olson, S. Franzen, and G. U. Nienhaus, *J. Am. Chem. Soc.* **127**, 40–41 (2005).
- <sup>54</sup>J. P. Ryckaert, G. Ciccotti, and H. J. C. Berendsen, *J. Comput. Phys.* **23**, 327 (1977).
- <sup>55</sup>M. Yoneya, H. J. C. Berendsen, and K. Hirasawa, *Mol. Simul.* **13**, 395 (1994).
- <sup>56</sup>M. Carducci, M. Pressprich, and P. Coppens, *J. Am. Chem. Soc.* **119**, 2669–2678 (1997).
- <sup>57</sup>N. Strickland and J. N. Harvey, *J. Phys. Chem. B* **111**, 841 (2007).
- <sup>58</sup>L. Cheng, I. Novozhilova, C. Kim, A. Kovalevsky, K. A. Bagley, P. Coppens, and G. B. Richter-Addo, *J. Am. Chem. Soc.* **122**, 7142 (2000).
- <sup>59</sup>N. Xu, J. Yi, and G. B. Richter-Addo, *Inorg. Chem.* **49**, 6253–6266 (2010).
- <sup>60</sup>K. Nienhaus, P. Palladino, and G. U. Nienhaus, *Biochemistry* **47**, 935 (2008).
- <sup>61</sup>I. Schlichting, J. Berendzen, G. Phillips, and R. Sweet, *Nature* **371**, 808–812 (1994).
- <sup>62</sup>E. A. Brucker, J. S. Olson, M. Ikeda-Saito, and G. N. Phillips, *Proteins: Struct., Funct., Bioinf.* **30**, 352 (1998).
- <sup>63</sup>C. E. Immoos, F. Sulc, P. J. Farmer, K. Czarniecki, D. F. Bocian, A. Levina, J. B. Aitken, R. S. Armstrong, and P. A. Lay, *J. Am. Chem. Soc.* **127**, 814 (2005).
- <sup>64</sup>Z. N. Zahran, L. Chooback, D. M. Copeland, A. H. West, and G. B. Richter-Addo, *J. Inorg. Biochem.* **102**, 216 (2008).
- <sup>65</sup>J. B. Aitken, S. E. Thomas, R. Stocker, S. R. Thomas, O. Takikawa, R. S. Armstrong, and P. A. Lay, *Biochemistry* **43**, 4892 (2004).
- <sup>66</sup>A. Giuffrè, E. Forte, M. Brunori, and P. Sarti, *FEBS Lett.* **579**, 2528 (2005).
- <sup>67</sup>D. M. Copeland, A. S. Soares, A. H. West, and G. B. Richter-Addo, *J. Inorg. Biochem.* **100**, 1413 (2006).
- <sup>68</sup>A. M. Rich, R. S. Armstrong, P. J. Ellis, and P. A. Lay, *J. Am. Chem. Soc.* **120**, 10827 (1998).
- <sup>69</sup>R. F. Tilton, I. D. Kuntz, and G. A. Petsko, *Biochemistry* **23**, 2849 (1984).
- <sup>70</sup>E. C. Liang, “Structural and functional analysis of proximal pocket mutants of sperm whale myoglobin,” Ph.D. thesis, Rice University, 1999.
- <sup>71</sup>P. Banushkina and M. Meuwly, *J. Phys. Chem. B* **109**, 16911 (2005).
- <sup>72</sup>M. Lim, T. Jackson, and P. Anfinrud, *Proc. Natl. Acad. Sci. U. S. A.* **90**, 5801–5804 (1993).
- <sup>73</sup>K. Kuczera, J. Lambry, J. Martin, and M. Karplus, *Proc. Natl. Acad. Sci. U. S. A.* **90**, 5805–5807 (1993).
- <sup>74</sup>T. Ho and H. Rabitz, *J. Chem. Phys.* **119**, 6433–6442 (2003).
- <sup>75</sup>S. Manzhos, X. Wang, R. Dawes, and T. Carrington, *J. Phys. Chem. A* **110**, 5295–5304 (2006).
- <sup>76</sup>J. Danielsson and M. Meuwly, *J. Phys. Chem. B* **111**, 218 (2007).
- <sup>77</sup>T. Nagy, J. Y. Reyes, and M. Meuwly, *J. Chem. Theory Comput.* **10**, 1366–1375 (2014).